European Journal of Mechanics / A Solids 120 (2026) 106285

Contents lists available at ScienceDirect

European Journal of Mechanics / A Solids

journal homepage: www.elsevier.com/locate/ejmsol

Full length article

Transient beating frequency: A marker for predicting basin escape[☆]

Giuseppe Habib [a,b,*], Oleg V. Gendelman [c]

[a] Department of Applied Mechanics, Faculty of Mechanical Engineering, Budapest University of Technology and Economics, Műegyetem rkp. 3, Budapest, H-1111, Hungary
[b] MTA-BME Lendület "Momentum" Global Dynamics Research Group, Budapest University of Technology and Economics, Hungary
[c] Faculty of Mechanical Engineering, Technion – Israel Institute of Technology, Haifa, Israel

ARTICLE INFO

Keywords:
Unstable periodic solution
Dynamic saddle
Critical slowing down
Early warning signals
Data-driven estimation
Model-free
Nonlinear dynamics

ABSTRACT

In nonlinear systems, escape from a safe basin constitutes a critical instability mechanism that often leads to catastrophic outcomes, such as structural collapse or ship capsize. In one of the possible (and, arguably, most dangerous) scenarios, the escape occurs when a transient perturbation displaces the system state across the stable manifold of a dynamic saddle in the phase space. Predicting the proximity to this boundary remains a significant challenge, especially in systems for which governing equations are unavailable. This paper introduces the transient beating frequency as a novel, data-driven marker for predicting basin escape. We demonstrate that when a system is perturbed close to the basin boundary but remains within the safe potential well, its transient slow-flow envelope exhibits a pronounced beating behavior. We analytically prove that this beating frequency decreases and intersects zero with a vertical tangent precisely at the amplitude of the unstable saddle. Exploiting this mathematical constraint, we develop an estimation algorithm to extrapolate the location of the saddle from a single, safe transient trajectory. The proposed methodology is validated through two diverse numerical case studies: a 2-DoF softening model of a floating offshore wind turbine, demonstrating practical applicability in capsize prediction, and a 21-DoF finite element model of a hardening clamped–clamped von Kármán beam, proving the method's scalability to high-dimensional systems. The results confirm that the algorithm successfully and accurately estimates the amplitude of the unstable periodic orbit using only localized transient data, establishing the decrease of the transient beating frequency as an effective early warning marker for predicting dynamic-saddle escapes in engineering systems.

1. Introduction

Dynamical integrity, also known as basin stability, is a fundamental concept for the safety and reliability assessment of nonlinear systems. Since stability in such systems is typically local rather than global, finite perturbations can force a system to leave its safe basin of attraction. This can lead to evolution toward undesirable attractors or unbounded divergence, ultimately compromising structural integrity (Rega and Lenci, 2008, 2015; Menck et al., 2013). Consequently, relying solely on linear stability analysis is insufficient for comprehensive safety assessments.

Mapping basins of attraction directly is computationally demanding (Lenci and Rega, 2019; Habib, 2021), and existing techniques often suffer from severe computational cost and memory limitations (Hsu, 2013; Belardinelli and Lenci, 2016; Sun et al., 2018). However, global dynamics is fundamentally organized by unstable solutions and their stable manifolds, which form the boundaries of these basins of attraction. Therefore, identifying unstable solutions often provides the critical information necessary to evaluate the dynamical integrity of the coexisting stable states (Strogatz, 2024; Thompson and Stewart, 2002; Genda et al., 2026).

In practice, identifying these unstable solutions is challenging. Analytical approaches, such as the multiple scales method (Nayfeh and Mook, 2024), averaging methods (Sanders et al., 2007; González-Carbajal et al., 2022), and harmonic balance (Mickens, 1984), can successfully identify unstable steady-state solutions, but they require explicit knowledge of the governing equations. Numerical continuation techniques, typically combining pseudo-arclength continuation with shooting methods (Nayfeh and Balachandran, 2008), are standard but equally model-dependent. Conversely, in experimental settings were numerical models are typical unavailable, the challenge is much greater. Control-based continuation methods (Barton et al., 2012; Raze et al., 2025) can track unstable branches, but they are hardware-intensive and require precise feedback control loops, limiting their

☆ This article is part of a Special issue entitled: 'Rega's 80th Birthday' published in European Journal of Mechanics / A Solids.

* Corresponding author.
E-mail address: habib@mm.bme.hu (G. Habib).

https://doi.org/10.1016/j.euromechsol.2026.106285
Received 23 March 2026; Received in revised form 17 June 2026; Accepted 9 July 2026
Available online 16 July 2026
0997-7538/

broader application. Alternatively, data-driven system identification techniques (Lin and Belardinelli, 2026; Cenedese et al., 2022) can be coupled with numerical methods to locate unstable solutions, though this remains an indirect approach.

To circumvent these limitations, recent methodologies have focused on estimating unstable solutions using solely transient dynamical data. A prominent marker in this context is the phenomenon of critical slowing down (Lim and Epureanu, 2011; Riso et al., 2020; Kadar et al., 2025; Habib, 2025). Because system dynamics naturally decelerates in the vicinity of steady-state solutions, tracking this slowing down allows for the prediction of nearby unstable states via extrapolation in either the parameter space (Lim and Epureanu, 2011; Riso et al., 2020; Kadar et al., 2025; Habib, 2023) or the phase space (Habib, 2025). However, these techniques have been predominantly developed for autonomous systems. One of the few exceptions for non-autonomous frameworks is the study by Chen and Epureanu (2018), which utilized Poincaré sections to forecast bifurcations in parametrically excited systems.

In this study, we explore a novel dynamic marker for estimating saddle-type unstable solutions in non-autonomous, harmonically forced systems: the beating frequency. Beating occurs due to the coexistence of different harmonics within an oscillating signal, resulting in a slow modulation of the amplitude envelope (further detailed in Section 3). To the authors' knowledge, the beating phenomenon has not previously been exploited for the prediction of unstable periodic solutions.

We focus on systems vulnerable to basin escape governed by a dynamic saddle, a topological feature frequently encountered across a wide array of engineering applications, from the capsizing of ships (Maki et al., 2022) to the pull-in instability of micro-electromechanical systems (MEMS) (Younis, 2011; Rega and Lenci, 2008; Ruzziconi et al., 2014). Such escape mechanisms can be phenomenologically captured by a single-degree-of-freedom harmonically excited Duffing oscillator exhibiting either a softening or hardening nonlinear stiffness (discussed in Section 2).

The primary objective of this study is to introduce and validate a novel framework that leverages variations in the beating frequency of transient trajectories to predict saddle escape mechanisms. Specifically, we demonstrate how this frequency-amplitude relationship can be utilized to estimate the location of saddle-type unstable periodic solutions, thereby identifying the boundary of a safe basin of attraction without requiring prior knowledge of the system's equations of motion. By establishing the fundamental phenomenology — supported by analytical exploration of the local saddle dynamics — this work provides a foundational theoretical basis for a new class of predictive methodologies. To demonstrate the robustness and versatility of the proposed approach, its predictive capabilities are validated on two distinct, highly nonlinear numerical systems: a two-degree-of-freedom floating offshore wind turbine model featuring a softening potential, and a finite-element model of a clamped–clamped von Kármán beam exhibiting a hardening potential.

2. Saddle escape mechanism

To illustrate the saddle escape mechanism, we consider a generic Duffing oscillator, whose dynamics is governed by the equation of motion

$$\ddot{x} + 2\zeta\dot{x} + x + \gamma x^3 = F\cos(\omega t), \tag{1}$$

where ζ is the damping ratio, F is the forcing amplitude, ω is the forcing frequency, t marks the time, and x is the system displacement. The coefficient γ dictates the type of nonlinearity. To illustrate the fundamental phenomenology of the escape mechanism, the remainder of this section focuses on a softening system ($\gamma = -1$), while the equivalent mechanism for a hardening system ($\gamma = +1$) will be addressed in Section 7. Dots $\dot{\bullet}$ indicate time derivatives. Without loss of generality, all quantities are assumed dimensionless.

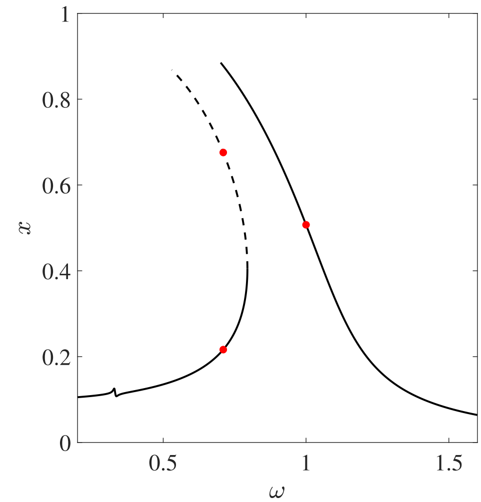

Fig. 1. Frequency response of the system in Eq. (1) for $\zeta = 0.01$ and $F = 0.1$. Solid line: stable periodic solutions, dashed lines: unstable periodic solutions. Red dots refer to the cases analyzed in Fig. 2. (For interpretation of the references to color in this figure legend, the reader is referred to the web version of this article.)

This system has been extensively studied (Kovacic and Brennan, 2011), and its dynamics, although very rich, is largely explored and well understood. Two main features are particularly relevant for this study. The first one is the bending of the frequency response curve toward excitation frequencies lower than the natural frequency, due to the softening nonlinearity. The practical consequence of this is the existence of a region in the parameter space where the system exhibits three coexisting periodic solutions: two stable solutions that are topologically separated by an unstable one of saddle type. The other one is the possibility of escape aperiodic diverging trajectories related to the negative stiffness for $|x| > 1$.

This phenomenon is visualized in Fig. 1, where the frequency response is depicted for the parameter values $\zeta = 0.01$ and $F = 0.1$. The branches of periodic solutions are disconnected because of the diverging trajectories for high amplitudes.

Extensive studies (Gendelman, 2018; Karmi et al., 2021; Kravetc et al., 2023) have illustrated that this system presents two main qualitatively different routes to escape its potential well, which are illustrated in Figs. 2a–c and 2d–f, respectively. When the system operates on the upper branch of periodic solutions (i.e., after resonance), generally only one stable periodic solution exists, apart from cases of subharmonic resonance (Raze and Kerschen, 2025). Small perturbations to the system from its steady-state periodic motion cause additional transient oscillations, which rapidly disappear, as illustrated in Fig. 2(a) ($\omega = 1$ and a perturbation amplitude of 0.1 in $\dot{x}$). Larger perturbations lead to larger transient oscillations, which might approach the region with negative stiffness ($|x| > 1$), as shown in Fig. 2(b) (velocity perturbation amplitude of 0.425). The time series depicted in Fig. 2(b) passes relatively close to $x = -1$, suggesting that a larger perturbation might lead to a basin escape. This is verified by the time series illustrated in Fig. 2(c), which was obtained through a perturbation only slightly larger than the one in Fig. 2(b) (velocity perturbation amplitude of 0.4251). This escape scenario, named *maximum mechanism* in Karmi et al. (2021), is relatively predictable, as the system gradually approaches the region of negative stiffness with increasing perturbation amplitudes.

For forcing frequencies below resonance, the escape scenario is significantly different. Let us consider the forcing frequency $\omega = 0.71$, for which the stable periodic solution coexists with an unstable periodic solution, as illustrated by the black lines in Fig. 3. In this case as well, a small perturbation causes only a transient effect, as depicted in Fig.

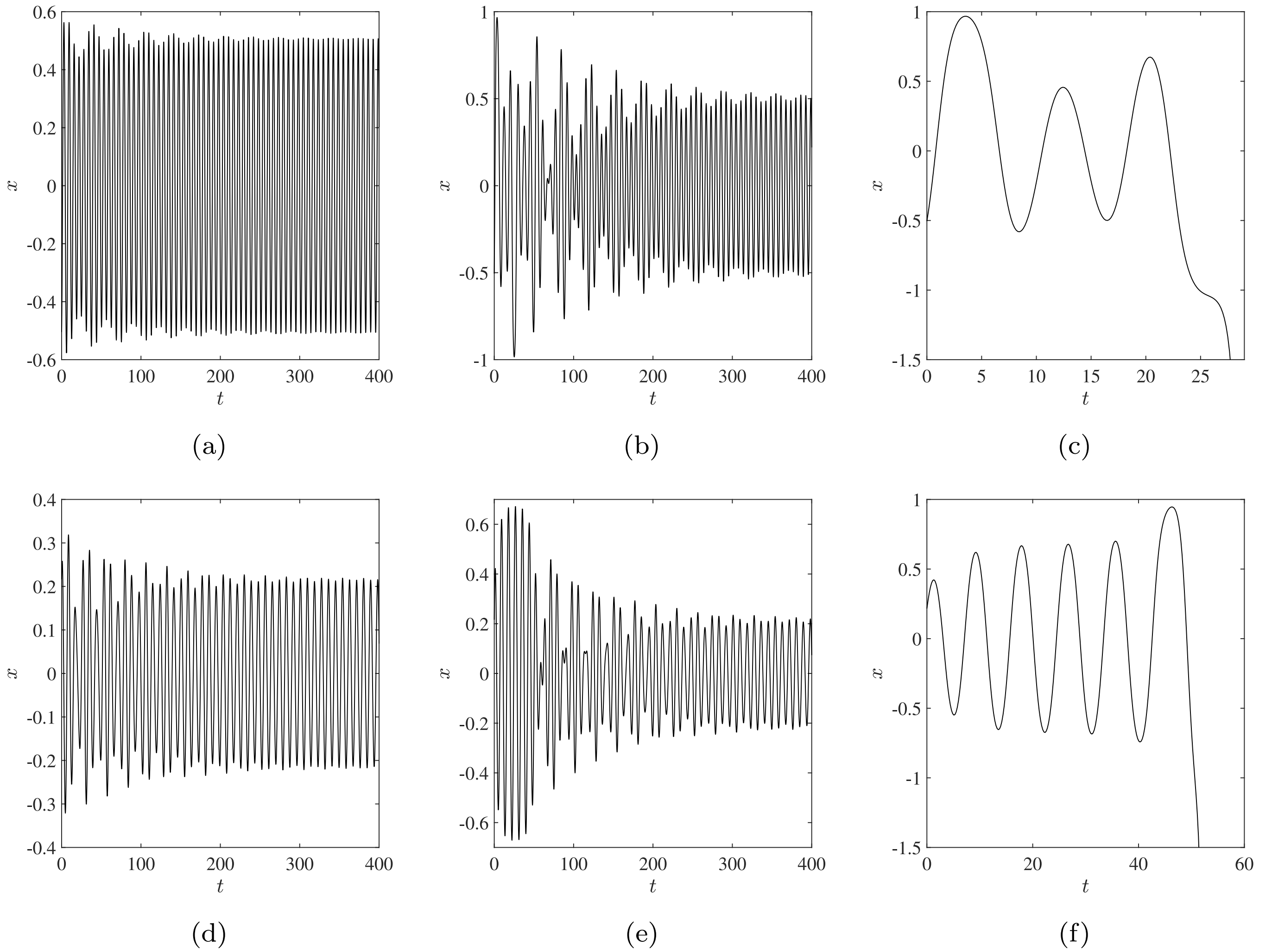

Fig. 2. Time series of the system in Eq. (1) for the parameter values $\zeta = 0.01$, $F = 0.1$ and either $\omega = 1$ (subplots (a)–(c)) or $\omega = 0.71$ (subplots (d)–(f)). Initial conditions obtained from perturbations in $\dot{x}$ from the steady-state condition of: (a) 0.1, (b) 0.4250, (c) 0.4251, (d) 0.1, (e) 0.2789, (f) 0.2790.

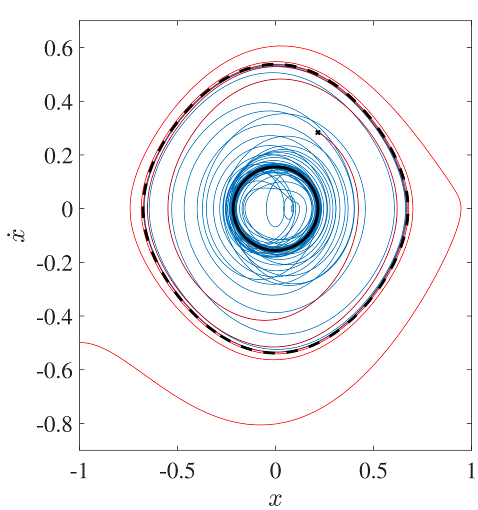

Fig. 3. Steady-state solutions of the system in Eq. (1) for $\zeta = 0.01$, $F = 0.1$ and $\omega = 0.71$. Solid black line: stable periodic solution, dashed black line: unstable periodic solution, thin blue line: trajectory corresponding to the time series in Fig. 2(e), thin red line: trajectory corresponding to the time series in Fig. 2(f), black crosses mark trajectories' initial conditions. (For interpretation of the references to color in this figure legend, the reader is referred to the web version of this article.)

2(d) (velocity perturbation of 0.1). Larger perturbations lead to larger transient oscillations, as shown in Fig. 2(e) for a velocity perturbation of 0.2789. We note that the time series in Fig. 2(e) has a maximal absolute amplitude of 0.6716, which is significantly lower than 1. However, a slightly larger perturbation (0.2790) causes the system to escape from the potential well. In this case, the escape is not related to a gradual approach to the region with negative stiffness, but rather to overcoming the saddle-type unstable periodic solution, which marks the boundary of the lower-amplitude stable periodic solution's basin of attraction. Once a trajectory passes the unstable periodic solution, its oscillation amplitude increases until it reaches the region with negative stiffness and diverges unboundedly. This scenario, which is named *saddle mechanism* in Karmi et al. (2021), is clearly illustrated in Fig. 3, where the blue line marks the trajectory converging to the periodic solution, while the red line indicates the one diverging. Both of them pass very close to the unstable periodic solution, but then diverge from each other as they belong to different basins of attraction.

We note that *overcoming* the unstable periodic solution is not precise terminology, but it is used solely to simplify the explanation. In fact, the system is three-dimensional; therefore, the unstable periodic solution does not fully bound the phase space, but rather lies on the boundary of the basin of attraction, which is formed by its stable manifolds. Since the basin boundaries are formed by the unstable periodic solution's stable manifolds, any trajectory initiated sufficiently close to the boundary is first attracted toward the unstable periodic solution, and is then repelled either toward the stable periodic solution or toward a basin escape.

In a practical monitoring problem, the former escape scenario ($\omega = 1$, Fig. 2a–2c) is much more predictable than the latter one ($\omega = 0.71$, Fig. 2d–2f), as the trajectory in Fig. 2(b) is clearly close to the negative stiffness region, delivering an obvious alert signal. Conversely, the one in Fig. 2(e) is relatively far from it and is hardly interpretable as critically dangerous. Assuming that the mathematical system under study is a simplified model of a real system, such as a floating wind turbine (see Section 6), estimating the proximity to a negative stiffness region is generally much easier than detecting an invisible unstable periodic solution.

While the analysis above focuses on a softening potential, it is important to note that a topologically equivalent saddle escape mechanism exists for hardening systems ($\gamma > 0$ in Eq. (1)). In such systems, the frequency response curve bends to the right, and the coexisting solutions and dynamic saddle emerge at excitation frequencies higher than the natural frequency. A practical example of this hardening escape mechanism will be explored in Section 7 through a clamped–clamped von Kármán beam. In that case, the escape scenario does not lead to aperiodic trajectories but to a large amplitude periodic solution.

We note that the system can escape from the potential well even through a gradual increase in the forcing amplitude, or by changing the excitation frequency and reaching resonance while keeping the system constantly in its steady-state conditions. However, these cases are not considered in the present study, which focuses strictly on saddle escape mechanism triggered by transient perturbations. When a system is perturbed close to the boundary of the saddle's stable manifold, its transient return to the stable attractor is characterized by a slow modulation of the oscillation amplitude. This phenomenon, known as beating, serves as the primary dynamic marker for our predictive method, as detailed in the following section.

3. Beating phenomenon

When a vibrating signal comprises two harmonic components with different but close frequencies, it exhibits the beating phenomenon. This is characterized by a slow modulation of the oscillation amplitude, resulting from alternating phases of constructive and destructive interference between the two harmonics. This phenomenon can be conveniently illustrated through a forced undamped linear oscillator, i.e.,

$$\ddot{x} + x = \cos(\omega t). \tag{2}$$

The solution of the system (assuming initial conditions at rest) is

$$x(t) = \frac{1}{1-\omega^2}\left(\cos(\omega t) - \cos(t)\right), \tag{3}$$

where the harmonic terms with frequencies ω and 1 correspond to the forced and free components of the solution, respectively. The solution can be reorganized into the form

$$x(t) = -\left(\frac{2}{1-\omega^2}\sin\left(\frac{\omega-1}{2}t\right)\right)\sin\left(\frac{\omega+1}{2}t\right), \tag{4}$$

where the $\sin((\omega+1)t/2)$ term represents the fast oscillation at the average frequency, while the slow envelope, defining the beat, is governed by the $\sin((\omega-1)t/2)$ term. This phenomenon is visualized in Fig. 4 for $\omega = 0.9$. The beating frequency is given by the difference between the system's natural frequency and the forcing frequency, which, in this case, is 0.1. Because of the linearity of the system, the beating frequency is unaffected by the oscillation amplitude (which depends on the initial conditions and the forcing amplitude) and is determined solely by the forcing frequency.

In the presence of relatively small linear damping, the phenomenon remains qualitatively similar. The primary difference is that the beating becomes a transient effect; as the free vibrations dissipate over time, the system asymptotically converges to the steady-state forced response.

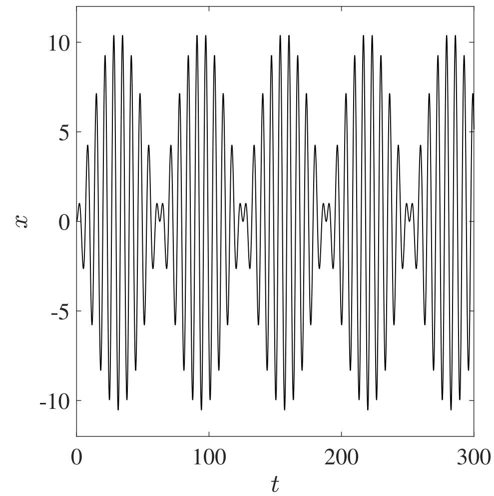

Fig. 4. Time series of the system in Eq. (2) for $\omega = 0.9$ and initial conditions at rest.

Additionally, in this damped scenario, the beating frequency is determined by the difference between the damped natural frequency and the forcing frequency. Note that the phenomenon is mostly relevant for dynamics close to the resonance, which are the main focus of this study.

The introduction of nonlinearity, as seen in the system governed by Eq. (1), significantly complicates the scenario. First, the natural frequency of a nonlinear system is amplitude-dependent, making the beating frequency amplitude-dependent as well. However, this effect alone does not qualitatively alter the fundamental beating mechanism. More importantly, the presence of an unstable solution has a profound effect on the beating frequency. During the constructive interference phase, the large-amplitude oscillatory motion approaches the unstable periodic solution, which locally slows down the system's dynamics and consequently lengthens the modulation period. From a theoretical standpoint, it is worth noting that this slowly varying beating amplitude corresponds precisely to the envelope dynamics established by the system's slow-flow (or averaged) equations. In established analytical theories of escape dynamics (Thompson, 1989), it is exactly the topology of these slow-flow equations — specifically the presence of equilibrium saddle points representing the unstable periodic solutions — that dictates the stability boundaries and the critical slowing down observed during the modulation.

This critical slowing down is clearly visible in the time series in Fig. 2(e), where the first beat — lasting up to approximately $t = 60$ — is significantly longer than the subsequent ones. To empirically extract this slow-flow envelope and better highlight the phenomenon, we apply a specific coordinate transformation. First, we introduce the coordinate ρ to track the oscillation amplitude, defined as

$$\rho = \sqrt{x(t)^2 + x(t-\tau)^2}, \tag{5}$$

where $\tau = \pi/(2\omega)$ is equivalent to one quarter of the forcing period. This specific delay is strategically chosen because, for a signal dominated by the frequency ω, the delayed signal $x(t-\tau)$ acts as an orthogonal phase component. Consequently, the Euclidean norm ρ effectively filters out the fast oscillations and provides a smooth, primary approximation of the slowly varying amplitude envelope. The resulting signal is illustrated in Fig. 5b. An additional advantage of this approach is that it does not require sampling both position and velocity, as is typically the case in practice. Next, the upper and lower envelopes of the $\rho(t)$ curve are extracted using the `envelope` function in MATLAB. This function calculates the envelopes based on the magnitude of the analytic signal, obtained by filtering the numerical signal with a Hilbert finite impulse

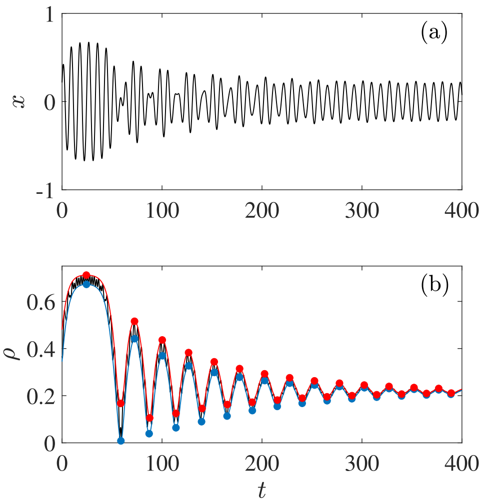

Fig. 5. (a) Time series of the system in Eq. (1) for $F = 0.1$, $\omega = 0.71$, $\zeta = 0.01$ and initial conditions $x(0) = 0.216$ and $\dot{x}(0) = 0.284$. (b) Black line: transformed signal in the ρ coordinate; red and blue lines mark the upper and lower envelopes of the curve. (For interpretation of the references to color in this figure legend, the reader is referred to the web version of this article.)

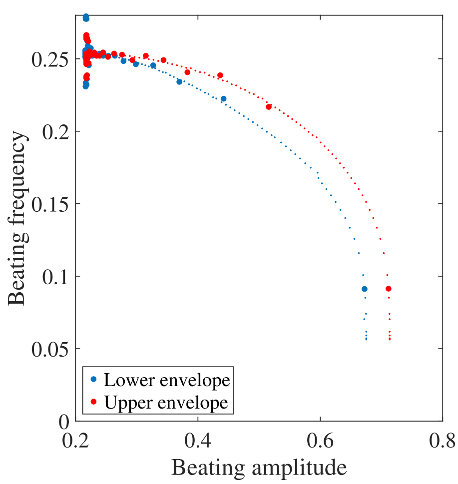

Fig. 6. Beating frequency vs. amplitude referred to the time series in Fig. 5 ($F = 0.1$, $\omega = 0.71$, $\zeta = 0.01$). Small dots are obtained through several time series of the undamped system, with changing initial conditions, serving as a theoretical reference. (For interpretation of the references to color in this figure legend, the reader is referred to the web version of this article.)

response (FIR) filter. The two resulting envelopes are represented in Fig. 5b by the red and blue lines.

We note that the envelopes could theoretically be computed directly from the original signal $x(t)$. However, applying the extraction to $\rho(t)$ provides superior results because the Hilbert FIR filter operates much more effectively on a signal where the primary carrier frequency has already been largely suppressed, leaving only widely spaced, low-amplitude, high-frequency residual harmonics.

By identifying the local maxima and minima of the two envelopes, the beating frequency can be characterized and plotted as a function of the oscillation amplitude. For each beat, the period is calculated as the time interval between the two bounding local minima, while the beat's amplitude is defined by the local maximum situated between them. The period of the first beat is estimated as twice the time difference between the first local maximum and the first local minimum. The results are represented by the large dots in Fig. 6, where the red and blue dots refer to the upper and lower envelopes, respectively.

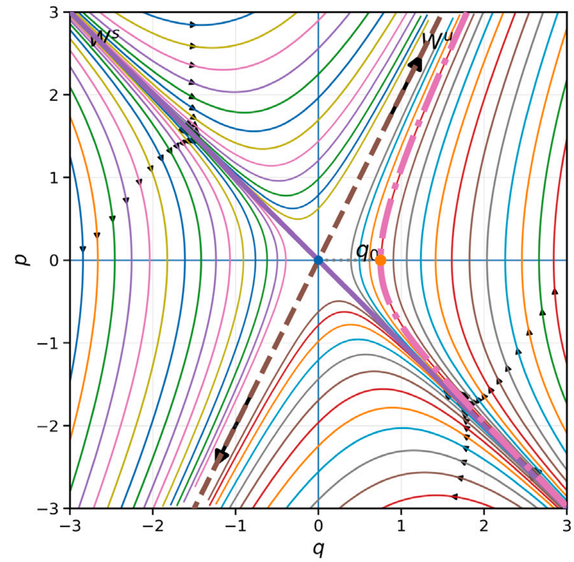

Fig. 7. Typical phase flow in the vicinity of a generic saddle. Violet and brown straight lines denote stable and unstable manifolds of the saddle, respectively. Purple curve denotes the sample phase trajectory with minimal distance q_0 from the saddle. (For interpretation of the references to color in this figure legend, the reader is referred to the web version of this article.)

To rigorously validate this frequency-amplitude relationship and establish a theoretical reference, we temporarily remove the damping from the system and perform several simulations with varying initial conditions. Because the undamped system does not experience transient decay, each simulation yields a steady, specific frequency-amplitude beating point. Computing this analysis produces the small dots shown in Fig. 6, which perfectly align with the data extracted from the single damped transient trajectory, verifying the underlying trend. It is important to emphasize that this numerical evaluation of the beating envelope — relying purely on delay embedding and signal processing — is entirely model-free and averaging-free. Unlike classical analytical techniques, which require the explicit derivation of slow-flow equations, the proposed extraction method is not bounded by the formal mathematical applicability of averaging theorems. This is a significant advantage, as establishing the strict validity of such theorems is often exceedingly difficult for complex, strongly nonlinear systems.

We note the monotonically decreasing trend of the two curves, which intersect the zero-frequency axis at the unstable periodic solution. This can be rapidly verified by referencing the unstable periodic solution depicted in Fig. 3 (dashed black line), whose maximal x value (0.676) closely matches the expected intersection of the blue line in Fig. 6 with the horizontal axis. The opposite extreme of the frequency-amplitude beating curves (occurring at the smallest beating amplitudes) corresponds to the stable periodic solution. The presence of a vertical tangent in the frequency-amplitude beating curves at zero frequency is a universal property of this saddle escape mechanism, as mathematically proven in Section 4.

Considering the physical properties and geometric constraints of the scenario described above, it becomes evident that the presence and amplitude of an unstable periodic solution can be predicted by analyzing the beating frequency of a single transient trajectory. The formulation of an algorithm to achieve this prediction is the primary focus of the remainder of this study.

4. Analytical derivation of the beating frequency near the saddle

As observed in Section 3, the beating frequency exhibits a monotonically decreasing trend, eventually intersecting the zero-frequency axis in correspondence with the unstable periodic solution. The empirical frequency-amplitude curves also exhibit a sudden drop as they approach this intersection, suggesting an asymptote with a vertical tangent. This section provides a rigorous mathematical proof of this property by analyzing the slow-flow modulation in the vicinity of the dynamic saddle.

Consider a generic saddle point on the phase plane. In the context of the current work, this is the phase plane of slow flow that describes the modulation of the recorded signal. Typical phase flow in the vicinity of the saddle point is depicted in Fig. 7.

Generically, the saddle fixed point has two real eigenvalues with opposite signs; we denote these eigenvalues as $\gamma_{1,2}$ with $\gamma_1 < 0 < \gamma_2$. Consequently, general solutions in the vicinity of the saddle are described by the following relationships:

$$q = C_1 e^{\gamma_1 t} + C_2 e^{\gamma_2 t}, \quad p = \dot{q} = C_1 \gamma_1 e^{\gamma_1 t} + C_2 \gamma_2 e^{\gamma_2 t}. \tag{6}$$

It is easy to exclude the time from Eq. (6) and obtain the well-known relationship for the family of the phase curves:

$$(q\gamma_2 - p)^{\gamma_2}(p - q\gamma_1)^{-\gamma_1} = \text{const.} \tag{7}$$

Expression (7) is formally valid for the sector $\{q > 0,\ q\gamma_1 < p < q\gamma_2\}$ between the branches of stable and unstable manifolds with positive q. For other sectors of the phase plane, expression (7) is also valid with appropriate sign adjustments. Consider a trajectory that passes at minimal distance q_0 from the saddle (cf. Fig. 7). Time of motion on the fragment of this curve near the saddle is evaluated as:

$$T = \int_L \frac{\mathrm{d}q}{p(q)}. \tag{8}$$

Here L denotes the fragment of the considered phase curve. We are interested in the asymptotic behavior of the time T as $q_0 \to 0$ and assume that the contribution of the rest of the phase trajectory is non-divergent. To obtain the basic approximation, it is sufficient to note that in the considered limit the denoted phase trajectory becomes close first to the stable manifold of the saddle $p - \gamma_1 q = 0$ and then to the unstable manifold $p - \gamma_2 q = 0$. Then, the contribution of these manifolds dominates in the integral (8), thus leading to the following expression:

$$T = -\left(\frac{1}{\gamma_2} - \frac{1}{\gamma_1}\right)\ln(q_0) + O(1). \tag{9}$$

More accurate asymptotic estimation of the integral (8) is indeed possible, but not necessary here, since the correction will be of the same (or smaller) asymptotic order as the rest of the phase trajectory.

Frequency of oscillations can be estimated as follows:

$$\Omega(q_0) \approx -\frac{2\pi|\gamma_1\gamma_2|}{(\gamma_2 - \gamma_1)\ln(q_0)}. \tag{10}$$

Approaching the saddle point amounts to the limit $q_0 \to 0$. In this limit, derivative of the frequency apparently diverges:

$$\frac{\mathrm{d}\Omega}{\mathrm{d}q_0} \approx \frac{2\pi|\gamma_1\gamma_2|}{(\gamma_2 - \gamma_1)q_0 \ln^2(q_0)}. \tag{11}$$

This expression rationalizes the vertical asymptote of the frequency–amplitude dependence as the amplitude approaches the dynamical saddle.

To bridge this local phase-plane analysis with the observable beating phenomenon, we note that the minimal distance q_0 in the slow-flow coordinates scales linearly with the physical envelope amplitude mismatch — specifically, the difference between the amplitude of the unstable periodic solution and the amplitude of the recorded transient envelope. Because the distance q_0 decreases as the physical amplitude increases toward the boundary, the derivative of q_0 with respect to the physical amplitude is strictly negative. Applying the chain rule, the positive divergence of $\mathrm{d}\Omega/\mathrm{d}q_0$ shown in Eq. (11) translates into a negative infinite derivative. Consequently, this directly implies the existence of the downward vertical tangent observed in the measurable frequency–amplitude curves as the system approaches the dynamical saddle.

5. Unstable periodic solution estimation

Let us assume that the exact equations of motion of a given system are unknown, but it is known that the system is topologically similar to the Duffing oscillator described in Eq. (1). This is a realistic premise for many engineering systems susceptible to dynamic-saddle basin escapes, such as floating offshore structures or MEMS (where the nonlinearity is usually of hardening type).

Consider the system subjected to a harmonic excitation slightly below its natural frequency (or above for a hardening system). While operating in its steady-state periodic motion, the system experiences a perturbation. This perturbation triggers a transient dynamics that, while significant, is insufficient to force the system out of its safe potential well. By analyzing the beating phenomenon experienced during this transient phase, we can compute the envelopes of the oscillation amplitude and plot the corresponding frequency-amplitude beating curves. By extrapolating these curves, we can estimate their intersections with the zero-frequency axis, which in turn provides an estimate of the unstable periodic solution's oscillation amplitude.

The procedure is first explained in detail and demonstrated using the softening Duffing oscillator considered thus far, with an excitation frequency of $\omega = 0.71$. For this estimation, data from three distinct transient trajectories are utilized. These time series are generated by applying velocity perturbations of 0.1, 0.13, and 0.16 to the system from its steady-state condition ($\zeta = 0.01$, $F = 0.1$).

For illustration, the trajectory corresponding to the largest perturbation (0.16) is represented in Fig. 8. The top panel of Fig. 8(a) shows the raw displacement time series (x), while a phase space projection of this trajectory is shown in Fig. 8(b).

To isolate the beating envelope, the time series is transformed into the amplitude coordinate ρ (represented by the black line in the bottom panel of Fig. 8(a)), from which the upper and lower envelopes are computed (red and blue lines, respectively). By identifying the local maxima and minima of these envelopes, we extract the discrete points that make up the frequency-amplitude beating curve. These are marked by the red dots (derived from the upper envelope) and blue dots (derived from the lower envelope) in Fig. 9(a).

Although the decreasing trend of the beating frequency with increasing amplitude is clearly visible, accurately estimating the exact intersection of these curves with the zero-frequency axis requires a tailored mathematical extrapolation. Based on the fundamental features of the frequency-amplitude beating curves illustrated previously (which were consistently encountered across varying parameter values), we constrain our estimation curve using the following characteristics:

- The curve decreases monotonically between the minimal beating amplitude (corresponding to the stable periodic solution) and the intersection with the zero-frequency axis (the unstable periodic solution), maintaining a strictly negative second derivative (concave downwards).
- The first derivative of the curve is zero at the minimal beating amplitude and $-\infty$ at the intersection with zero frequency.

It is important to emphasize that while the zero derivative at the minimal amplitude is a heuristic constraint based on phenomenological observations, the vertical tangent ($-\infty$ derivative) at the zero-frequency intersection is a fundamental, universal property of the dynamic saddle, as proven analytically in Section 4. Furthermore, the monotonically decreasing, downward-concave trend is characteristic of systems where no secondary nonlinear phenomena alter the envelope dynamics.

For the purpose of the estimation algorithm, let f denote the beating frequency, f_0 the beating frequency in the immediate vicinity of the stable periodic solution, a the beating amplitude, a_0 the beating amplitude at the periodic solution, and a_u the critical beating amplitude at the intersection with the zero-frequency axis. Our objective is to estimate a_u, which dictates the amplitude of the unstable periodic solution.

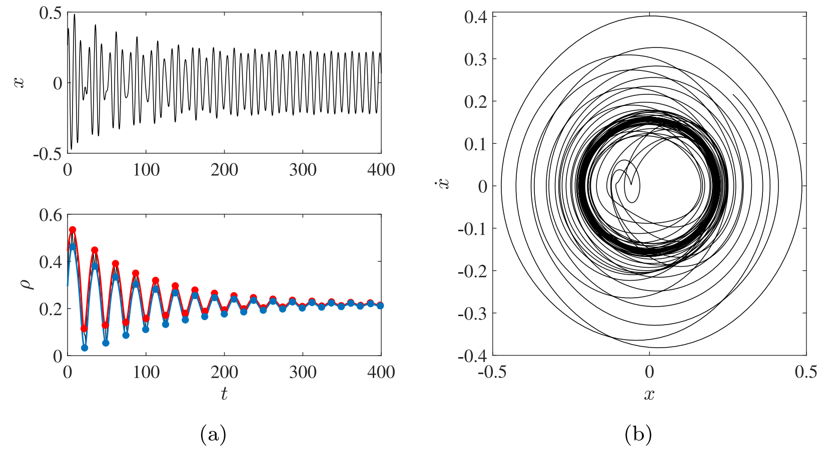

Fig. 8. (a) Time series of the system in Eq. (1) for $F = 0.1$, $\omega = 0.71$, $\zeta = 0.01$ and initial conditions obtained through a velocity perturbation of 0.16 from the stable periodic solution; top: displacement (x); bottom: amplitude of oscillation (ρ, black line), lower and upper envelopes of ρ (blue and red lines, respectively), where blue and red dots mark the local maxima and minima. (b) Trajectory in the phase space. (For interpretation of the references to color in this figure legend, the reader is referred to the web version of this article.)

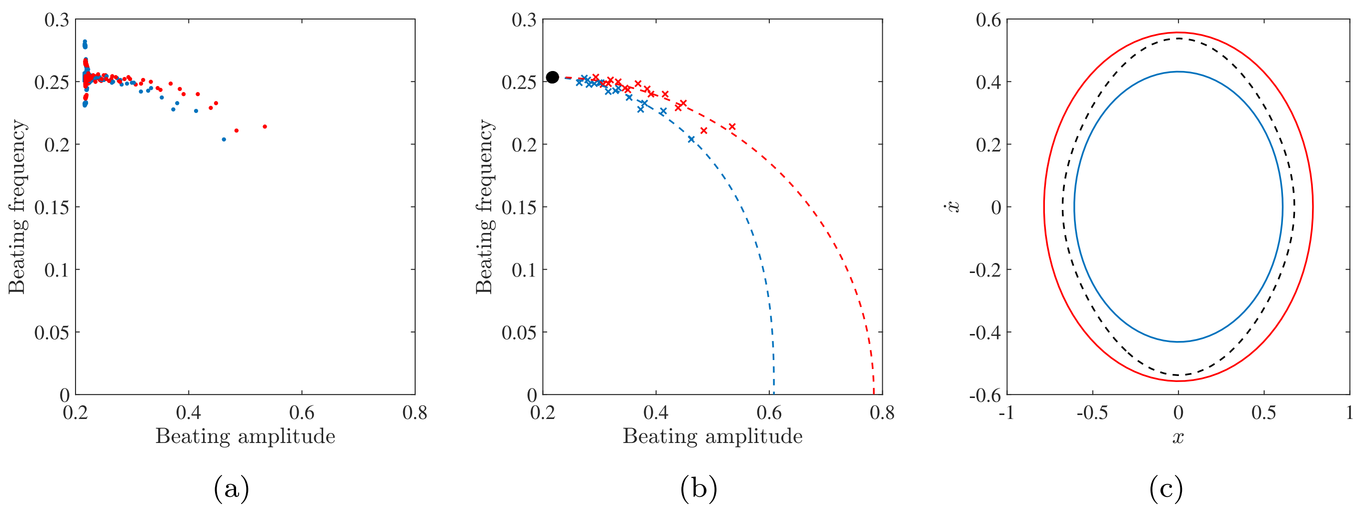

Fig. 9. (a) Relation between the beating amplitude and frequency obtained from the local minima and maxima of Fig. 8a and similar trajectories; blue dots: lower envelope, red dots: upper envelope. (b) Estimated trends of the beating frequency-amplitude curves. (c) Blue and red lines: estimated unstable periodic solutions (through lower and upper envelopes); dashed black line: reference analytical unstable solution. (For interpretation of the references to color in this figure legend, the reader is referred to the web version of this article.)

To perform the extrapolation, the following function is introduced:

$$f = f_0 \left(1 - g(a; p_1, p_3, p_4)\right)^{p_2}, \tag{12}$$

where

$$g = \frac{\tilde{a}^{p_1}}{1 + p_3 (1 - \tilde{a})^{p_4}} \quad \text{and} \quad \tilde{a} = \frac{a - a_0}{a_u - a_0}, \tag{13}$$

with $a \in \left[a_0,\ a_u\right]$ such that $\tilde{a} \in [0,\ 1]$. Additionally, the parameters are bounded such that $p_1 > 1$ and $0 < p_2 < 1$. The exponent $p_2 < 1$ guarantees that the derivative of the function approaches $-\infty$ as $\tilde{a} \to 1$, correctly enforcing the analytically proven vertical tangent at the saddle. It is important to emphasize that this empirical function is a power-law interpolation rather than the exact logarithmic relation derived in Section 4. Attempting to regress exact logarithmic singularities from sparse, discrete transient data is numerically highly unstable. Furthermore, the local expansion derived in Section 4 is valid strictly in the asymptotic limit approaching the saddle and does not naturally capture the zero slope characteristic of the dynamics near the stable periodic solution ($a \to a_0$). Consequently, the interpolating function is strategically constructed to bridge these two physical regimes. By enforcing a horizontal tangent at the safe baseline while preserving the analytically proven vertical tangent at the escape boundary, the function ensures a robust numerical estimation of a_u without strictly conforming to the exact analytical form.

While setting $p_3 = 0$ would mathematically satisfy the basic curve characteristics mentioned above, the parameters p_3 and p_4 are included to provide the function with the flexibility necessary to accurately adapt to the empirical data points. To promote a regular, smooth trend, additional constraints are applied during the optimization: $1.2 < p_1 < 2.5$, $1/4 < p_2 < 1/2$, $p_3 > 0$, $p_4 > 1$, and $p_2 \cdot p_4 < 1$. The final condition ensures the curve maintains a strictly negative second derivative.

The estimation algorithm proceeds as follows (repeated independently for both the upper and lower envelopes):

1. Identify a_0 as the final recorded beating amplitude of the trajectory, when the system has practically converged to the stable periodic solution.
2. Estimate f_0 as the average of the last 10 beating frequency values recorded (these (a_0, f_0) anchor points are marked by the black dots in Fig. 9(b)).
3. Select the first 5 frequency-amplitude beating points recorded from each trajectory — i.e., those corresponding to the highest

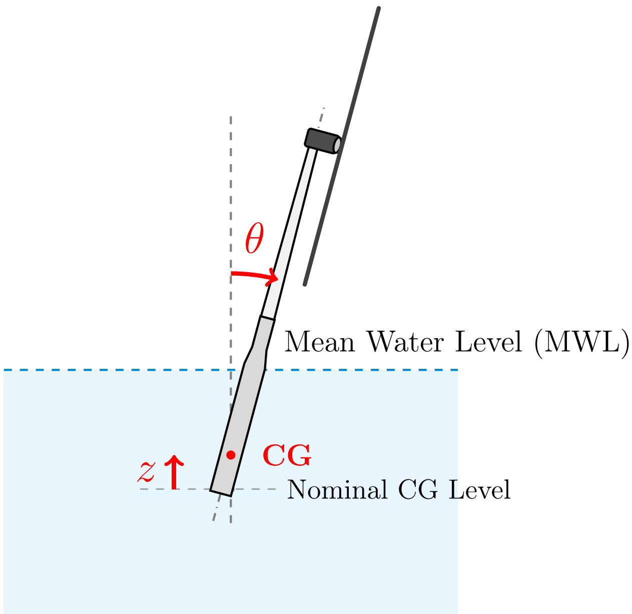

Fig. 10. Scaled schematic of the modified "Short-Spar" floating offshore wind turbine model subject to external excitation. The figure illustrates the rigid-body heave (z) and pitch (θ) degrees of freedom, showing the system displaced from its nominal center of gravity (CG) level and mean water level. Mooring lines are omitted in the figure.

amplitudes, which are closest to a_u (marked by the blue and red crosses in Fig. 9(b)).

4. Implement a least-squares minimization algorithm to identify the values of p_1, p_2, p_3, p_4, and a_u that best fit the selected high-amplitude beating points while satisfying the established mathematical constraints. To avoid converging on local minima, this optimization is performed by executing the `MATLAB` `fminsearch` function multiple times with randomized initial parameter guesses. `fminsearch` exploits the simplex search method developed by Lagarias et al. (1998). The optimally fitted curves are depicted by the dashed blue and red lines in Fig. 9(b).
5. Utilize the identified a_u values to construct elliptic estimates of the unstable periodic orbit in the phase space, assuming a primary harmonic oscillation frequency of ω.

We note that the procedure can also be applied to the velocity signal of the system instead of the position, leading to equivalent results.

For the specific case under study, the identified parameters for the lower envelope are:

$$p_1 = 1.796,\ p_2 = 0.3754,\ p_3 \approx 0,$$
$$p_4 = 1.9214,\ a_u = 0.6074, \tag{14}$$

and for the upper envelope:

$$p_1 = 1.9401,\ p_2 = 0.4995,\ p_3 \approx 0,$$
$$p_4 = 1.673,\ a_u = 0.7845. \tag{15}$$

We note that, for this particular trajectory, p_3 and p_4 proved to be practically irrelevant to the overall trend of the curves.

The resulting estimated unstable periodic orbits are represented by the blue and red lines in Fig. 9(c). The exact, analytically derived unstable solution is marked by the black dashed line, which fits neatly between the two estimated bounds, thus validating the relative accuracy of the estimation procedure.

While a single transient trajectory could theoretically suffice for this estimation, utilizing data points from multiple perturbations — particularly those yielding larger transient amplitudes — significantly mitigates estimation errors caused by noise or signal irregularities. As explored further in the Conclusions section, relying on the extrapolation of a vertical asymptote makes the algorithm sensitive to sudden drops in the signal. Furthermore, the algorithm inherently projects the estimated unstable solution as an ellipse in the phase space, which serves as a highly functional, but fundamentally approximate, boundary for real-time predictive monitoring.

Table 1
System parameters for the modified 2-DOF "Short-Spar" model. Derivations are detailed in Appendix.

Parameter	Symbol	Value	Unit
Inertial Properties			
Total Heave Mass	M_{33}	4.92×10^6	kg
Total Pitch Inertia	M_{55}	2.10×10^{10}	kg m^2
Stiffness & Coupling			
Heave Linear Stiffness	K_{z1}	3.45×10^5	N/m
Heave Asymmetry	K_{z2}	5.00×10^3	N/m^2
Pitch Linear Stiffness	$K_{\theta 1}$	2.10×10^8	N m/rad
Pitch Softening	$K_{\theta 3}$	1.00×10^9	N m/rad^3
Pitch-to-Heave Coupling	α	8.76×10^6	N/rad^2
Heave-to-Pitch Coupling	β	1.17×10^7	N/rad
Damping			
Heave Damping	B_{33}	2.00×10^5	N s/m
Pitch Damping	B_{55}	5.00×10^6	N m s/rad

6. Case study 1: Floating offshore wind turbine

To evaluate the forecasting capabilities of the proposed method on a representative engineering system, we consider the dynamics of a floating offshore wind turbine (Fig. 10). The system is based on the OC3-Hywind spar-buoy, a standard benchmark in offshore engineering (Jonkman, 2010). This platform is particularly relevant for basin escape analysis because it exhibits a distinct capsize instability governed by a softening potential well, topologically similar to the Duffing oscillator but embedded within a coupled multi-DoF framework.

Only the heave (z) and pitch (θ) DoFs are considered in the model. The governing equations of motion are given by:

$$\mathbf{M}\ddot{\mathbf{q}} + \mathbf{C}\dot{\mathbf{q}} + \mathcal{R}(\mathbf{q}) = \mathbf{F}_{\mathrm{ext}}(t), \tag{16}$$

where $\mathbf{q} = [z, \theta]^T$ is the state vector. The mass matrix $\mathbf{M} = \mathrm{diag}(M_{33}, M_{55})$ includes both the structural mass and the hydrodynamic added mass, $\mathbf{C}$ is the damping matrix, $\mathcal{R}(\mathbf{q})$ provides the nonlinear restoring forces, and $\mathbf{F}_{\mathrm{ext}}(t)$ represents the interaction of the buoy with the sea waves, modeled as an external harmonic excitation.

A critical feature of this model is the nonlinear interaction between the degrees of freedom. While the OC3-Hywind is often linearized for control applications, modeling the large-amplitude dynamics relevant to capsize requires a nonlinear formulation. We adopt the coupling structure proposed in Jingrui et al. (2010), which has been extensively used in the literature (Davidson and Kalmár-Nagy, 2020; Habib et al., 2022) and accounts for the geometric variation of the submerged volume and the center of buoyancy. The restoring force vector components in $\mathcal{R}(\mathbf{q})$ are defined as:

$$\mathcal{R}_z(z, \theta) = K_{z1} z + K_{z2} z^2 - \alpha \theta^2 \tag{17}$$

$$\mathcal{R}_\theta(z, \theta) = K_{\theta 1} \theta - K_{\theta 3} \theta^3 - \beta z \theta \tag{18}$$

Here, the pitch restoring moment includes a linear term $K_{\theta 1}$ (hydrostatic stability) and a cubic softening term $K_{\theta 3}$, calibrated to represent the loss of righting moment at large inclination angles. The heave stiffness includes a quadratic term K_{z2} representing the asymmetric response of the mooring system (hardening in tension, slackening in compression).

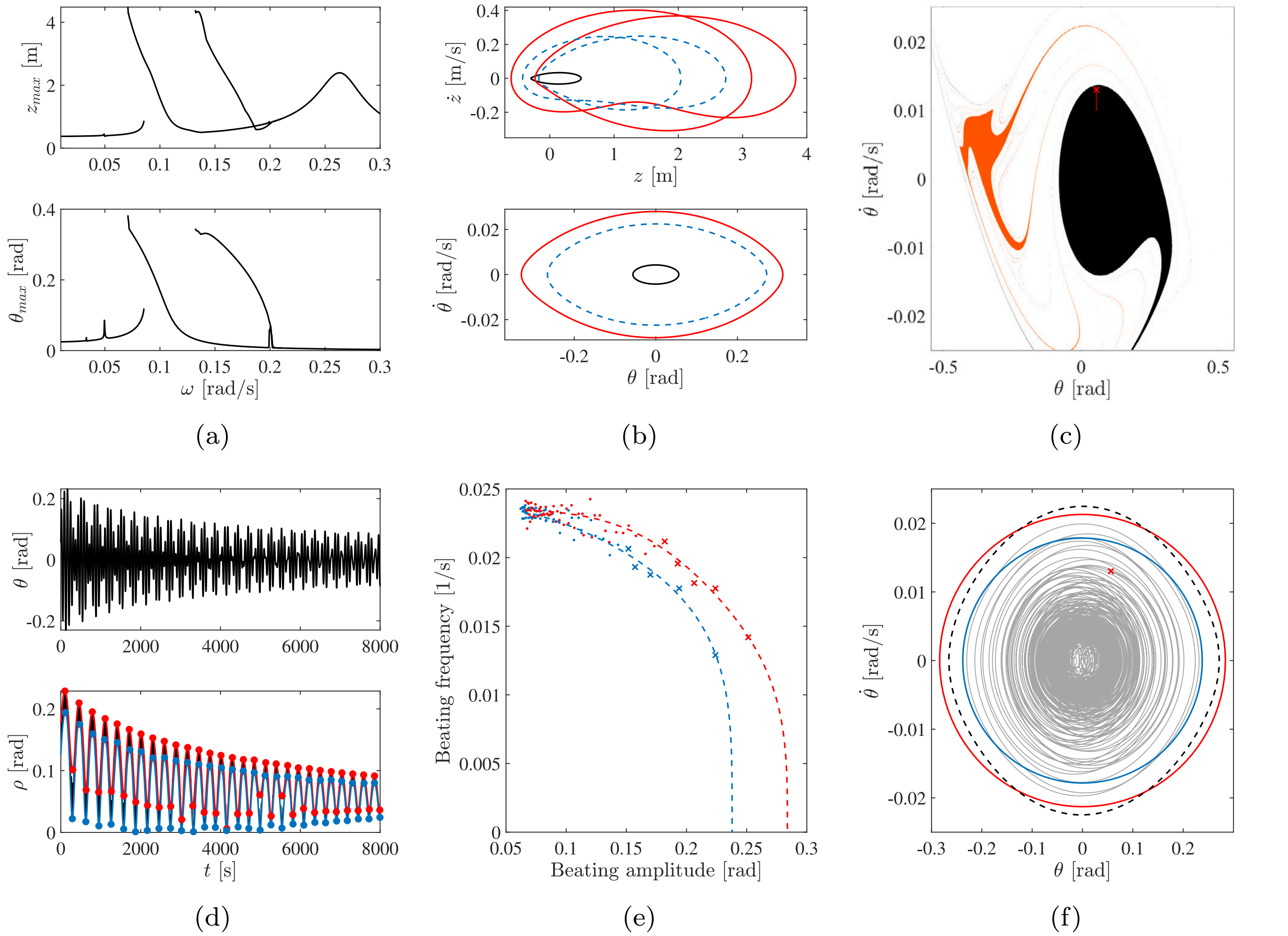

Fig. 11. (a) Frequency response of the floating wind turbine model. (b) Coexisting steady-state solutions for $\omega = 0.075$ rad/s; dashed lines mark the unstable solution. (c) Basins of attraction in the θ-$\dot{\theta}$ space, with $z(0) = 0.486$ m and $\dot{z}(0) = 0.0021$ m/s (pinned to the small-amplitude solution, perturbations applied only in θ and $\dot{\theta}$); the white region leads to capsizing, and the red cross denotes the initial condition of the trajectory used for estimation. (d) Time series for the estimation (*top*) and its transformed signal in polar coordinates (*bottom*); initial conditions are on the small-amplitude attractor with a perturbation in $\dot{\theta}$ of 0.013 rad/s. (e) Beating frequency-amplitude curves; crosses: points used for the estimation, dots: points not used, dashed lines: estimated curves, blue: lower envelope, red: upper envelope. (f) Dashed line: reference (exact) unstable periodic solution, blue and red lines: estimated unstable solutions from lower and upper envelopes, respectively, gray line: trajectory used for the estimation, red cross: initial point of the trajectory. (For interpretation of the references to color in this figure legend, the reader is referred to the web version of this article.)

The coupling terms $-\alpha\theta^2$ and $-\beta z\theta$ introduce a nonlinear energy transfer mechanism: the former represents the change in vertical buoyancy due to inclination, while the latter represents the modulation of the metacentric height by heave displacement (Jingrui et al., 2010). Unlike in Jingrui et al. (2010), Davidson and Kalmár-Nagy (2020), Habib et al. (2022), we exclude the external parametric wave elevation term to focus strictly on the stability boundaries under direct harmonic excitation.

The standard OC3-Hywind design features natural periods in heave and pitch that are relatively close (~30 s), leading to complex internal resonances. To ensure that the forecasting method is validated on the saddle–node escape topology without the interference of strong modal interactions, we adopt a modified "short-spar" configuration. We reduce the platform draft from the original 120 m (Jonkman, 2010) to 70 m. This modification serves a dual purpose: physically, it aligns the model with modern commercial trends toward shallower-draft spars optimized for port assembly; methodologically, it detunes the system by separating the natural frequencies to $\omega_z \approx 0.27$ rad/s and $\omega_\theta \approx 0.10$ rad/s (a ratio of ~ 2.7).

The system parameters, scaled physically from Jonkman (2010) to maintain consistency with the reduced geometry, are summarized in Table 1. Detailed derivations of the mass scaling and hydrostatic coefficients are provided in Appendix.

The system is subjected to monochromatic wave excitation with a force amplitude of $F_{\text{amp}} = 1.25 \times 10^5$ N and a moment amplitude of $M_{\text{amp}} = 5.0 \times 10^6$ Nm, corresponding roughly to a wave amplitude of $A \approx 0.5$ m. The phase difference between the two forcing components is neglected, a simplification deemed acceptable for the scope of this paper. As the frequency response diagram in Fig. 11(a) demonstrates, this forcing level is sufficient to trigger significant nonlinear effects. In particular, the softening behavior characterizing the resonance in pitch (~ 0.10 rad/s) is clearly visible. Additionally, the diagram exhibits superharmonic resonances at $\omega = 0.033$ and $\omega = 0.05$ rad/s, related to the cubic and quadratic terms $K_{z2}z^2$ and $-K_{\theta 3}\theta^3$, respectively, as well as subharmonic resonances for $\omega \in (0.13, 0.2)$ rad/s, which exhibit a period twice that of the forcing period. This latter phenomenon is due to the coupling term $-\beta z\theta$, which triggers a Mathieu-type parametric instability. We note that the frequency response diagram in Fig. 11(a) was obtained through direct numerical simulations performing

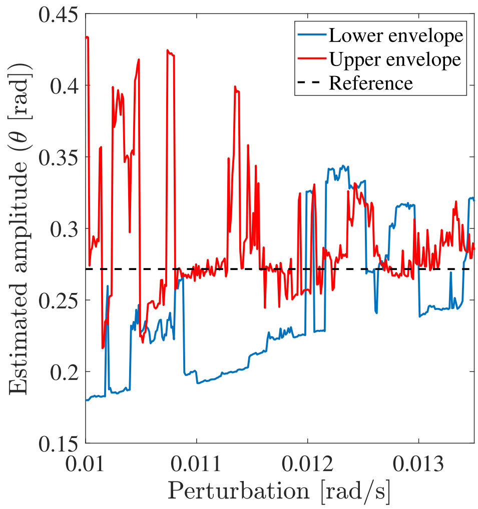

Fig. 12. Estimated amplitude of the unstable solution for different perturbation amplitude. Parameter values are the same as for Fig. 11.

several frequency sweeps up and down with various initial conditions; accordingly, only stable solutions are depicted.

Although the system dynamics is very rich, we focus our attention on the 1:1 resonance in pitch at $\omega = 0.075$ rad/s. Here, the system presents two stable periodic solutions, a large- and a small-amplitude one, separated by an unstable periodic solution, as depicted in Fig. 11(b). We note that, although the unstable solution and the large attractor exhibit a double winding in heave during each period, they do not undergo period doubling, unlike the subharmonic branch observed for $\omega \in (0.13, 0.2)$ rad/s. The basins of attraction for the two competing stable solutions are illustrated in Fig. 11(c), where the black and red areas refer to the small- and large-amplitude solutions, respectively, while the white area indicates initial conditions leading to capsize. This cross-section of the basin of attraction was obtained by fixing the initial conditions for z and $\dot{z}$ to those of the small-amplitude solution, and varying the perturbations exclusively in θ and $\dot{\theta}$. The reference unstable periodic solution (dashed blue line in Fig. 11(b)) was obtained by initiating a trajectory almost exactly on the basin of attraction boundary (its stable manifold) and letting the system approach and dwell near the unstable saddle. Then, one forcing period was sampled and a periodicity condition was validated within a given threshold. Obviously, proceeding with the simulation, this trajectory would have eventually reached either one of the two attractors or lead to capsizing.

Our objective is to estimate the unstable periodic orbit lying on the boundary of the basin of attraction of the small-amplitude solution, using only the information provided by a transient trajectory initiated within the safe basin. We initiate a trajectory by imposing a velocity perturbation of $\dot{\theta} = 0.013$ rad/s from the small-amplitude periodic solution, resulting in the state vector $\mathbf{q}(0) = [0.486, 0.0565, 0.0021, 0.0130]^T$ (marked by the red cross in Fig. 11(c)). The resulting time series for the pitch coordinate θ is illustrated in the top panel of Fig. 11(d).

For the estimation analysis, only the pitch coordinate is utilized, while the heave dynamics is ignored. On the one hand, this is a mathematical necessity, as the proposed 1D envelope method cannot directly process multiple coupled coordinates simultaneously. On the other hand, this constraint accurately reflects a common, practical monitoring scenario where only a specific subset of a system's degrees of freedom is accessible for experimental measurement.

The trajectory is transformed into the amplitude coordinate ρ using the delay embedding described in Eq. (5), and the upper and lower envelopes are computed, as marked by the red and blue lines in the bottom panel of Fig. 11(d). From the local maxima and minima of the envelopes, the discrete frequency-amplitude beating points are

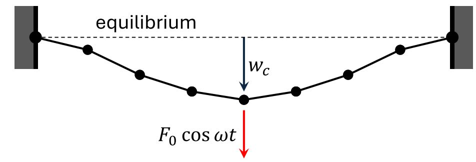

Fig. 13. Finite element discretization of the von Kármán beam model.

extracted, as plotted in Fig. 11(e). The cluster of points at low beating amplitudes is used to estimate the baseline beating frequency and amplitude in the vicinity of the stable periodic solution, denoted as f_0 and a_0, respectively. Subsequently, the 5 peaks with the largest amplitudes for each envelope (the crosses in Fig. 11(e)) are used to estimate the frequency-amplitude beating curves, represented by the dashed red and blue lines.

The least-squares minimization procedure yielded the following parameters for the upper envelope:

$$p_1 = 1.21,\ p_2 = 0.265,\ p_3 = 4.67,\ p_4 = 3.78,\ a_u = 0.284, \tag{19}$$

and for the lower envelope:

$$p_1 = 1.21,\ p_2 = 0.250,\ p_3 \approx 0,\ p_4 = 4.00,\ a_u = 0.238. \tag{20}$$

The projections of the two estimated unstable periodic solutions are represented in Fig. 11(f) by the red and blue lines, which successfully bracket the amplitude of the unstable solution (marked by the black dashed line). However, its maximal velocity is underestimated by the algorithm. This mismatch highlights one of the algorithm's intrinsic limitations: it approximates the unstable solution as an exact ellipse, where the ratio between the maximal displacement and velocity is directly given by the forcing frequency, which is not strictly satisfied in nonlinear systems. We note that, although the trajectory used for the estimation is initiated close to the basin boundary (see the red cross in Fig. 11(c)), it does not pass infinitesimally close to the unstable solution, as is recognizable in Fig. 11(f) when comparing the gray solid line (the trajectory) to the black dashed line (the exact saddle). Nevertheless, the method accurately captures the location and scale of the unstable boundary.

To evaluate the robustness of the method, we repeat the estimation for different perturbation amplitudes, with the results represented in Fig. 12. The initial conditions relative to the different perturbation amplitudes are also marked by the red line in Fig. 11(c). The lines in Fig. 12 illustrate how the prediction accuracy tends to increase as the basin of attraction boundary is approached, which is not surprising because the beating frequency decrement is significant only for trajectories transiting very near the unstable solution. We also note that the blue and red lines are very irregular. This irregularity is related to the intrinsic difficulty of estimating a vertical asymptote, an operation which is very sensitive to even minor uncertainties.

7. Case study 2: von Kármán clamped–clamped beam

To demonstrate the versatility of the proposed methodology, the second case study considers a large dimensional system exhibiting a hardening nonlinearity. Specifically, we analyze a finite element (FE) model of a von Kármán beam with clamped–clamped boundary conditions (Fig. 13). The modeling framework is analogous to the one adopted by Jain et al. (2018) for simply supported beams, and closely follows the formulation in Habib et al. (2025), which utilizes identical boundary conditions but a higher spatial resolution.

The FE model accounts for moderate deformations by including quadratic terms in the kinematic formulation. The beam is discretized into 8 elements. Cubic shape functions are employed for the transverse deflection, while linear shape functions are used for the axial displacement. Since each of the 9 nodes possesses 3 degrees of freedom

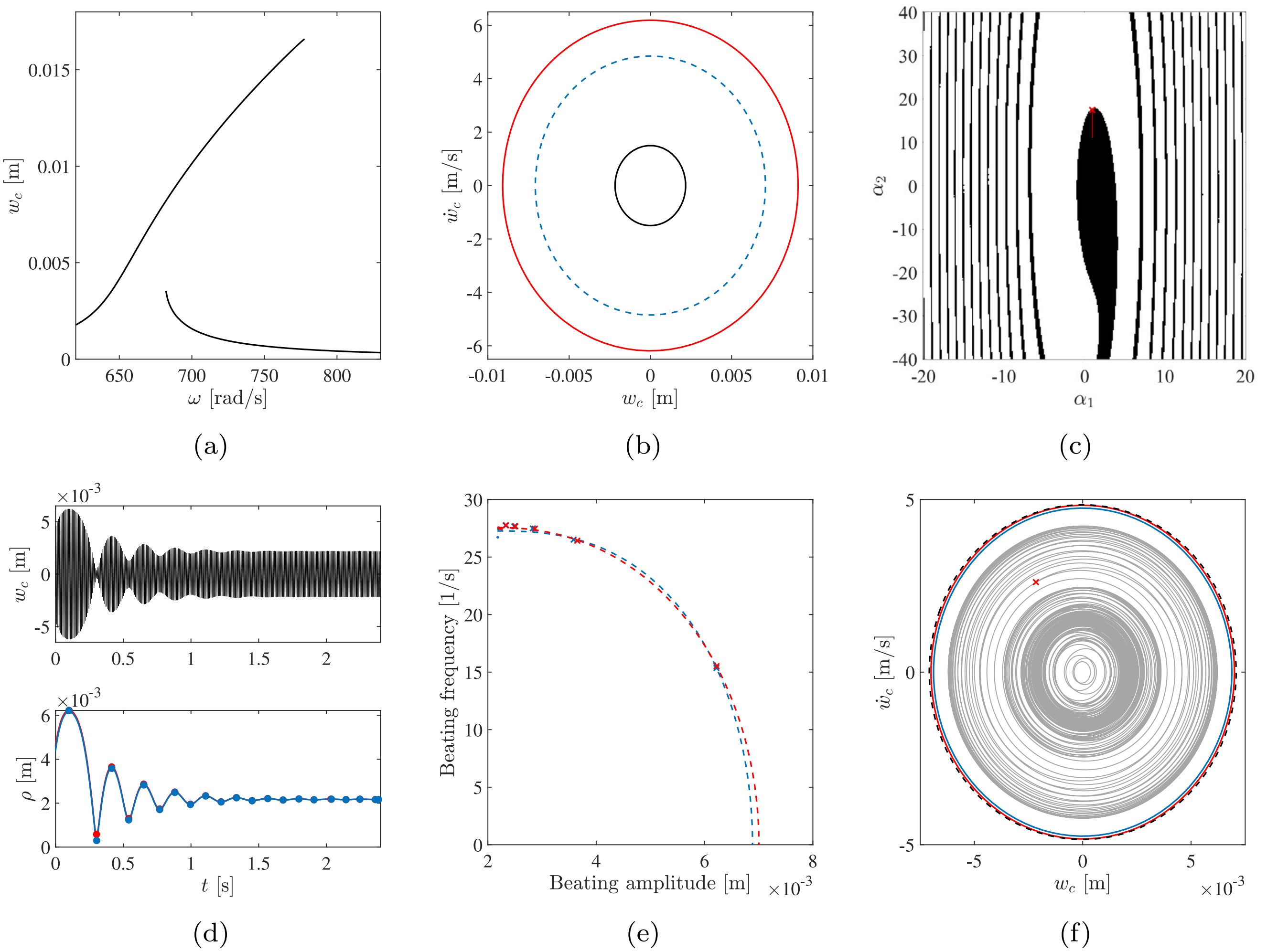

Fig. 14. (a) Frequency response of the von Kármán beam. (b) Coexisting steady-state solutions for $\omega = 690$ rad/s; dashed lines mark the unstable solution. (c) Basins of attraction in the α_1-α_2 space; black region: low amplitude attractor, white region: large amplitude attractor, red cross: initial condition of the trajectory used for estimation. (d) Time series for the estimation (*top*) and its transformed signal in polar coordinates (*bottom*); initial conditions: $\alpha_1 = 1$, $\alpha_2 = 17.5$. (e) Beating frequency-amplitude curves; crosses: points used for the estimation, dots: points not used, dashed lines: estimated curves, blue: lower envelope, red: upper envelope. (f) Dashed line: reference (exact) unstable periodic solution, blue and red lines: estimated unstable solutions from lower and upper envelopes, respectively, gray line: trajectory used for the estimation, red cross: initial point of the trajectory. (For interpretation of the references to color in this figure legend, the reader is referred to the web version of this article.)

(longitudinal displacement, transverse displacement, and rotation), and the clamped–clamped boundaries strictly constrain the 6 DoFs at the two ends, the resulting global system possesses 21 independent DoFs.

The dynamics of the discretized beam is governed by the matrix differential equation:

$$\mathbf{M}\ddot{\mathbf{u}} + \mathbf{C}\dot{\mathbf{u}} + \mathbf{K}\mathbf{u} + \mathbf{f}_{\mathrm{nl}}(\mathbf{u}, \dot{\mathbf{u}}) = \mathbf{F}(t), \tag{21}$$

where $\mathbf{u}$ is the 21×1 generalized displacement vector, and the overdot denotes the derivative with respect to time. $\mathbf{M}$, $\mathbf{C}$, and $\mathbf{K}$ represent the 21×21 mass, damping, and linear stiffness matrices, respectively. The vector $\mathbf{f}_{\mathrm{nl}}(\mathbf{u}, \dot{\mathbf{u}})$ encapsulates the nonlinear restoring and damping forces. Due to the von Kármán kinematic assumptions, which account for membrane stretching induced by transverse deflections, this nonlinear vector contains terms that are quadratic and cubic in the generalized displacements. Finally, $\mathbf{F}(t)$ represents the external harmonic excitation vector. For additional details regarding the mathematical formulation of the problem, we refer the interested reader to Jain et al. (2018).

The beam is assumed to be made of aluminum with the following physical properties: length 1 m, width 5 cm, thickness 2 cm, Young's modulus 70 GPa, density 2700 kg/m^3, and a Poisson ratio of 0.3. The material damping modulus is set to 10^6 Pa s. Based on these parameters, the two slowest natural frequencies of the discretized system are $\omega_1 = 657.77$ rad/s and $\omega_2 = 1814.2$ rad/s. The frequency ratio is approximately 2.758, which excludes the occurrence of strong internal modal interactions.

We note that the reduced number of elements used in the present discretization (8 elements), with respect to the same structure studied in Habib et al. (2025) (12 elements), practically does not affect the first natural frequency value, which has a difference of only 0.008%. Large amplitude solutions near resonance have a marginal difference of about 2.5% at the investigated amplitude. Conversely, higher natural frequencies and vibration modes are significantly affected by the coarser mesh. However, they are not relevant for the present analysis. Therefore, this reduced accuracy does not compromise the topological validity or the meaningfulness of the dynamical results. Crucially, the reduced 21-DoF model significantly accelerates the computational effort, making the extensive numerical calculation of the system's basins of attraction feasible. Furthermore, successfully applying the predictive algorithm to a 21-DoF system proves that the methodology scales effectively to high-dimensional problems, provided that modal interactions do not affect the dynamics.

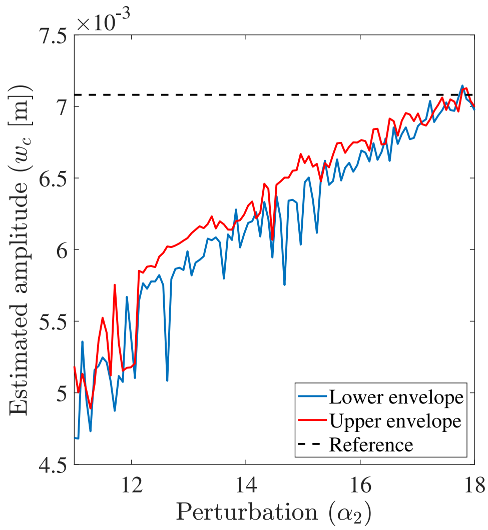

Fig. 15. Estimated amplitude of the unstable solution for different perturbation amplitude. Parameter values are the same as for Fig. 14.

Because the beam is not pre-compressed, it presents no buckling phenomena and exhibits a purely hardening geometric nonlinearity (equivalent to $\gamma > 0$ in the generic Duffing in Eq. (1)). The structure is excited by a harmonic point force of 1 N amplitude applied vertically at its center.

The frequency response of the system around the first resonance is illustrated in Fig. 14(a) (where unstable solutions are omitted). This diagram, obtained through direct numerical simulations encompassing forward and backward frequency sweeps, distinctly shows the peak bending to the right, characteristic of a strong hardening behavior.

We focus the analysis on the multi-valued region to the right of the first natural frequency by fixing the excitation frequency at ω = 690 rad/s. As illustrated in Fig. 14(b), at this frequency, the system presents two coexisting stable periodic solutions: a small-amplitude attractor (black line) and a large-amplitude one (red line), which are topologically separated by an unstable periodic solution of saddle type (dashed blue line).

The objective is to estimate the amplitude of this unstable periodic solution utilizing only a transient trajectory that eventually converges to the small-amplitude attractor.

To systematically select initial conditions and visualize the basin of attraction, we slice the 42-dimensional phase space. Let $\mathbf{q}_{\mathrm{ref}} = [\mathbf{u}_{\mathrm{ref}}^{\intercal}, \mathbf{v}_{\mathrm{ref}}^{\intercal}]^{\intercal}$ represent the full 42-element state vector of a point lying exactly on the small-amplitude periodic solution at a specific initial forcing phase (where $\mathbf{u}$ encompasses the 21 displacements and $\mathbf{v}$ the 21 velocities). We define perturbed initial conditions using two scalar multipliers, α_1 and α_2, such that $\mathbf{q}(0) = [\alpha_1\mathbf{u}_{\mathrm{ref}}^{\intercal}, \alpha_2\mathbf{v}_{\mathrm{ref}}^{\intercal}]^{\intercal}$. Setting $\alpha_1 = \alpha_2 = 1$ places the system perfectly on the small-amplitude attractor. A section of the basin of attraction in the α_1-α_2 parameter space is shown in Fig. 14(c), where the black and white areas mark the basins of the small- and large-amplitude solutions, respectively.

We extract a transient trajectory initiated within the safe basin, marked by the red cross in Fig. 14(c) ($\alpha_1 = 1$ and $\alpha_2 = 17.5$). The resulting time series is shown in Fig. 14(d). The upper panel illustrates the transverse deflection at the center of the beam, denoted as w_c, that is the only quantity collected from the time series; conversely, the bottom panel shows the transformed signal in the polar amplitude coordinate ρ. In this case, the upper and lower envelopes (red and blue lines) are remarkably close to each other. This occurs because the steady-state solutions at this operating point closely resemble perfect ellipses in the phase space, with negligible contributions from higher harmonics.

By identifying the local maxima and minima of the envelopes in the bottom panel of Fig. 14(d), we obtain the discrete frequency–amplitude beating points marked by crosses and dots in Fig. 14(e). Utilizing the identical least-squares minimization procedure applied in the previous case study, we extrapolate the frequency–amplitude beating curves, represented by the dashed lines.

The optimization yielded the following parameters for the upper envelope:

$$p_1 = 2.15,\ p_2 = 0.498,\ p_3 = 0.0045,\ p_4 = 1.25,$$
$$a_u = 0.0070, \tag{22}$$

and for the lower envelope:

$$p_1 = 2.5,\ p_2 = 0.499,\ p_3 = 0.0217,\ p_4 = 1.79,$$
$$a_u = 0.0069. \tag{23}$$

The estimated unstable periodic solutions corresponding to these a_u values are plotted in Fig. 14(f). The analytical unstable solution (black dashed line) is very accurately captured by both the lower (blue line) and upper (red line) estimates, which practically overlap. We emphasize that, although the transient trajectory used for the estimation was initiated very close to the basin boundary (red cross in Fig. 14(c)), the actual trajectory in the phase space (gray line in Fig. 14(f)) does not pass extremely close to the unstable periodic solution itself. Despite this, the algorithm successfully extracts the necessary dynamical footprint to achieve a highly accurate saddle estimation in a 21-DoF nonlinear system.

Also for this system, we investigate the accuracy of the estimation for variations of the perturbation amplitude, which is represented in Fig. 15. The initial conditions relative to the different perturbations are marked by the red line in Fig. 14(c). Differently from the floating wind turbine model, in this case the upper and lower envelope provide similar amplitude values, which is probably due to the absence of any modal interaction and limited presence of superharmonics. Both lines consistently underestimate the unstable periodic solution amplitude, approaching the real value as initial conditions are closer to the basin of attraction boundary. This estimation error, although not negligible, is conservative with respect to safety. Also in this case, the curves present irregularities, but not as marked as for the floating wind turbine model.

8. Conclusions

In this study, a novel methodology for estimating the location of saddle-type unstable periodic solutions in non-autonomous, harmonically excited systems was proposed and validated. By exploiting the transient beating phenomenon, we demonstrated that the beating frequency undergoes a critical slowing down, dropping logarithmically to zero as the oscillation amplitude approaches the unstable periodic solution. An analytical proof was provided to establish that the frequency-amplitude curve inherently features a vertical tangent at this intersection. This mathematical constraint served as the foundation for a predictive, least-squares estimation algorithm. The proposed data-driven method successfully predicted the unstable solution bounding the basin of attraction, without requiring prior knowledge of the governing equations of motion. The framework was rigorously validated across different topological scenarios, including a generic softening Duffing oscillator, a coupled two-degree-of-freedom floating offshore wind turbine model, and a finite-element model of a clamped–clamped von Kármán beam exhibiting hardening nonlinearity.

The potential of this approach lies primarily in its application as an early-warning predictive tool for structural health and safety monitoring. In many critical engineering applications — such as the capsizing of ships or the pull-in of MEMS — basin escape occurs suddenly and without an obvious gradual approach toward a negative stiffness region. By tracking the variation in beating frequency from a safe, transient perturbation, the proposed method provides a tangible measure of the system's proximity to dynamic-saddle escape, functioning as a real-time monitor for dynamical integrity.

Despite its predictive capabilities, the current formulation has several notable limitations. First, the estimation algorithm fundamentally identifies an amplitude, which is then converted to a periodic orbit by assuming an elliptical shape; this assumption generally does not hold for strongly nonlinear systems. Second, estimating the exact location of the unstable solution relies on extrapolating a vertical asymptote. Because the slope of the curve approaches infinity at this intersection, any minor uncertainty in capturing the sudden drop in beating frequency can translate into a disproportionately large error in the estimated amplitude (Studnicka, 1987). Consequently, the algorithm is inherently sensitive to measurement noise or signal irregularities. Furthermore, obtaining a high-accuracy estimate requires the measured transient trajectory to be initiated relatively close to the basin boundary; data points recorded far from the saddle exhibit a nearly flat frequency trend, which is largely uninformative for accurately pinning down the precise location of the asymptote. Finally, the presence of strong local nonlinearities, topological non-smoothness, or other secondary dynamical irregularities can distort the envelope dynamics, leading the erroneous estimation curves. This vulnerability to unexpected local dynamics is a well-known, inherent limitation of algorithms that rely on the phase- or parameter-space extrapolation of specific dynamical features (Lim and Epureanu, 2011; Habib, 2025).

Future work will focus on addressing these limitations and expanding the framework's applicability. A primary objective is the experimental validation of the method to rigorously test its robustness against real-world measurement noise. Additionally, the theoretical framework should be extended to accommodate more complex dynamical scenarios. This includes forecasting basin escapes governed by other types of dynamic saddles, such as quasiperiodic or chaotic invariant sets, as well as investigating the impact of strong modal interactions on the beating envelope. Finally, further studies will explore the adaptation of this predictive tool for systems subjected to periodic but non-monoharmonic excitations, ultimately formalizing the approach into a robust, iterative real-time diagnostic algorithm.

CRediT authorship contribution statement

Giuseppe Habib: Writing – original draft, Visualization, Software, Methodology, Investigation, Funding acquisition, Formal analysis, Data curation, Conceptualization. **Oleg V. Gendelman:** Writing – review & editing, Supervision, Investigation, Formal analysis.

Code availability

The data and the code utilized for generating the presented results are available from the author upon request.

Availability of data and material

Not applicable.

Funding

The research reported in this paper has been supported by Project number 2025-1.2.7-HU-CN-PARTNER-2025-00004 provided by the Ministry of Culture and Innovation of Hungary from the National Research, Development and Innovation Fund (GH) and by the Israel Science Foundation (grant 3085/25) (OG).

Declaration of competing interest

The authors declare that they have no known competing financial interests or personal relationships that could have appeared to influence the work reported in this paper.

Acknowledgments

The authors acknowledge the Erasmus+ project for supporting the logistical cooperation aspects required for this study.

Appendix. Derivation of floating wind turbine's parameters

This appendix details the derivation of the coefficients for the floating offshore wind turbine model. The baseline parameters are obtained from the OC3-Hywind definition report (Jonkman, 2010). The modification involves reducing the platform draft from $L_{\text{old}} = 120$ m to $L_{\text{new}} = 70$ m while maintaining the hull diameter $D = 6.5$ m to preserve the waterplane area.

A.1. Inertial properties

The total mass matrix includes both structural mass and hydrodynamic added mass. To ensure physical consistency during scaling, these components must be treated separately. The structural mass scales with the submerged volume (draft), while the heave added mass depends on the cross-sectional geometry (which remains constant).

Heave Mass (M_{33}): The original system mass is $M_{tot} = 8.23 \times 10^6$ kg. Based on the base diameter $D_{\text{base}} = 9.4$ m, the heave added mass is approximated as a hemisphere: $A_{33} \approx (2/3)\pi\rho(D_{\text{base}}/2)^3 \approx 0.28 \times 10^6$ kg. The original structural mass is thus $M_{\text{struct}}^{\text{old}} = M_{tot} - A_{33} = 7.95 \times 10^6$ kg. Scaling the structural mass linearly with draft:

$$M_{\text{struct}}^{\text{new}} = M_{\text{struct}}^{\text{old}} \times \frac{70}{120} \approx 4.64 \times 10^6 \text{ kg}. \tag{A.1}$$

The total heave mass for the short spar is the sum of the scaled structural mass and the constant added mass:

$$M_{33} = 4.64 \times 10^6 + 0.28 \times 10^6 = 4.92 \times 10^6 \text{ kg}. \tag{A.2}$$

Pitch Inertia (M_{55}): Rotational inertia scales with the mass times the square of the characteristic length ($I \propto ML^2$). Since $M \propto L$, the inertia scales approximately with L^3. Using the original pitch inertia $M_{55}^{\text{old}} \approx 1.06 \times 10^{11}$ kg m^2:

$$M_{55} \approx M_{55}^{\text{old}} \times \left(\frac{70}{120}\right)^3 \approx 2.10 \times 10^{10} \text{ kg m}^2. \tag{A.3}$$

A.2. Stiffness and coupling coefficients

The hydrostatic stiffness and coupling terms depend on the waterplane area ($A_{cwl} = \pi(6.5/2)^2 \approx 33.18$ m^2) and the vertical geometry.

Linear Stiffness: The heave stiffness K_{z1} is determined by the waterplane area density ($\rho g A_{cwl}$) and remains unchanged from the OC3 value of 3.45×10^5 N/m. The pitch stiffness $K_{\theta 1}$ is tuned to achieve the target natural frequency $\omega_\theta = 0.10$ rad/s, required for frequency separation:

$$K_{\theta 1} = M_{55}\omega_\theta^2 = (2.10 \times 10^{10})(0.10)^2 = 2.10 \times 10^8 \text{ N m/rad}. \tag{A.4}$$

Physically, this corresponds to a metacentric height (GM) of approximately 4.5 m.

Nonlinear Coupling: The coupling coefficients are derived from the geometric formulation in Habib et al. (2022), scaled by the new characteristic lengths. The center of mass depth is scaled to $L_{SC} = 90 \times (70/120) = 52.5$ m, and the draft is $L_{draft} = 70$ m.

$$\alpha = \frac{1}{2}\rho g A_{cwl} L_{SC} \approx 8.76 \times 10^6 \text{ N/rad}^2 \tag{A.5}$$

$$\beta = \frac{1}{2}\rho g A_{cwl} L_{draft} \approx 1.17 \times 10^7 \text{ N/rad}. \tag{A.6}$$

A.3. Damping and forcing

Hydrodynamic damping is scaled geometrically with respect to the values in Jonkman (2010), and then slightly increased to regularize the motion. Heave damping (B_{33}) scales linearly with draft (L), while pitch damping (B_{55}) scales with L^3, yielding the values 2.00×10^5 N s/m and 5.00×10^6 N m s/rad, respectively.

The external forcing amplitudes correspond to a regular wave with amplitude $A_{wave} = 0.5$ m. Using the excitation coefficients at resonance ($\omega \approx 0.1$ rad/s) from the OC3 report (Jonkman, 2010):

$$F_{\rm amp} \approx (2.5 \times 10^5\,{\rm N/m}) \times 0.5\,{\rm m} = 1.25 \times 10^5\,{\rm N} \tag{A.7}$$

$$M_{\rm amp} \approx (1.0 \times 10^7\,{\rm Nm/m}) \times 0.5\,{\rm m} = 5.0 \times 10^6\,{\rm Nm}. \tag{A.8}$$

Data availability

Data will be made available on request.

References

Barton, D.A., Mann, B.P., Burrow, S.G., 2012. Control-based continuation for investigating nonlinear experiments. J. Vib. Control 18 (4), 509–520.
Belardinelli, P., Lenci, S., 2016. An efficient parallel implementation of cell mapping methods for mdof systems. Nonlinear Dynam. 86 (4), 2279–2290.
Cenedese, M., Axås, J., Bäuerlein, B., Avila, K., Haller, G., 2022. Data-driven modeling and prediction of non-linearizable dynamics via spectral submanifolds. Nat. Commun. 13 (1), 872.
Chen, S., Epureanu, B., 2018. Forecasting bifurcations in parametrically excited systems. Nonlinear Dynam. 91 (1), 443–457.
Davidson, J., Kalmár-Nagy, T., 2020. A real-time detection system for the onset of parametric resonance in wave energy converters. J. Mar. Sci. Eng. 8 (10), 819.
Genda, A., Fidlin, A., Gendelman, O.V., 2026. Basins of attraction and dynamic integrity in 1-DoF autonomous systems with quadratic drag.
Gendelman, O., 2018. Escape of a harmonically forced particle from an infinite-range potential well: a transient resonance. Nonlinear Dynam. 93 (1), 79–88.
González-Carbajal, J., García-Vallejo, D., Domínguez, J., 2022. Stability of a nonideally excited duffing oscillator. Nonlinear Dynam. 110 (4), 3075–3095.
Habib, G., 2021. Dynamical integrity assessment of stable equilibria: a new rapid iterative procedure. Nonlinear Dynam. 106 (3), 2073–2096.
Habib, G., 2023. Predicting saddle–node bifurcations using transient dynamics: a model-free approach. Nonlinear Dynam. 111 (22), 20579–20596.
Habib, G., 2025. Unstable limit cycle estimation from small perturbations: a minimal-data-driven approach. Nonlinear Dynam. 113 (13), 15725–15740.
Habib, G., Cenedese, M., Rega, G., 2025. Spectral submanifold reduction of high dimensional nonlinear systems for dynamical integrity analysis. Nonlinear Dynam. 113 (21), 28983–29005.
Habib, G., Giorgi, G., Davidson, J., 2022. Coexisting attractors in floating body dynamics undergoing parametric resonance. Acta Mech. 233 (6), 2351–2367.
Hsu, C.S., 2013. Cell-to-Cell Mapping: A Method of Global Analysis for Nonlinear Systems. Springer Science & Business Media.
Jain, S., Tiso, P., Haller, G., 2018. Exact nonlinear model reduction for a von kármán beam: slow-fast decomposition and spectral submanifolds. J. Sound Vib. 423, 195–211.
Jingrui, Z., Yougang, T., Wenjun, S., 2010. A study on the combination resonance response of a classic spar platform. J. Vib. Control 16 (14), 2083–2107.
Jonkman, J., 2010. Definition of the Floating System for Phase IV of OC3. Tech. Rep., National Renewable Energy Laboratory, Golden, CO (United States), pp. 500–47535.
Kadar, F., Stepan, G., Habib, G., 2025. Model-free fold bifurcation prediction from pre-bifurcation scenario: experimental validation through wheel shimmy vibrations. Nonlinear Dynam. 113 (10), 11247–11258.
Karmi, G., Kravetc, P., Gendelman, O., 2021. Analytic exploration of safe basins in a benchmark problem of forced escape. Nonlinear Dynam. 106 (3), 1573–1589.
Kovacic, I., Brennan, M.J., 2011. The Duffing Equation: Nonlinear Oscillators and their Behaviour. John Wiley & Sons.
Kravetc, P., Gendelman, O., Fidlin, A., 2023. Resonant escape induced by a finite time harmonic excitation. Chaos: An Interdiscip. J. Nonlinear Sci. 33 (6).
Lagarias, J.C., Reeds, J.A., Wright, M.H., Wright, P.E., 1998. Convergence properties of the nelder–mead simplex method in low dimensions. SIAM J. Optim. 9 (1), 112–147.
Lenci, S., Rega, G., 2019. Global Nonlinear Dynamics for Engineering Design and System Safety, vol. 588, Springer.
Lim, J., Epureanu, B.I., 2011. Forecasting a class of bifurcations: Theory and experiment. Phys. Rev. E—Statistical, Nonlinear, Soft Matter Phys. 83 (1), 016203.
Lin, B., Belardinelli, P., 2026. Sparse identification of quasipotentials via a combined data-driven method. Nonlinear Dynam. 114 (2), 124.
Maki, A., Miino, Y., Umeda, N., Sakai, M., Ueta, T., Kawakami, H., 2022. Nonlinear dynamics of ship capsizing at sea. Nonlinear Theory its Appl. IEICE 13 (1), 2–24.
Menck, P.J., Heitzig, J., Marwan, N., Kurths, J., 2013. How basin stability complements the linear-stability paradigm. Nat. Phys. 9 (2), 89–92.
Mickens, R., 1984. Comments on the method of harmonic balance. J. Sound Vib. 94 (3), 456–460.
Nayfeh, A.H., Balachandran, B., 2008. Applied Nonlinear Dynamics: Analytical, Computational, and Experimental Methods. John Wiley & Sons.
Nayfeh, A.H., Mook, D.T., 2024. Nonlinear Oscillations. John Wiley & Sons.
Raze, G., Abeloos, G., Kerschen, G., 2025. Experimental continuation in nonlinear dynamics: recent advances and future challenges. Nonlinear Dynam. 113 (6), 4949–4997.
Raze, G., Kerschen, G., 2025. A two-harmonic homotopy method to experimentally uncover isolated resonances. Mech. Syst. Signal Process. 232, 112670.
Rega, G., Lenci, S., 2008. Dynamical integrity and control of nonlinear mechanical oscillators. J. Vib. Control 14 (1-2), 159–179.
Rega, G., Lenci, S., 2015. A global dynamics perspective for system safety from macro-to nanomechanics: Analysis, control, and design engineering. Appl. Mech. Rev. 67 (5), 050802.
Riso, C., Ghadami, A., Cesnik, C.E., Epureanu, B.I., 2020. Data-driven forecasting of postflutter responses of geometrically nonlinear wings. AIAA J. 58 (6), 2726–2736.
Ruzziconi, L., Ramini, A.H., Younis, M.I., Lenci, S., 2014. Theoretical prediction of experimental jump and pull-in dynamics in a mems sensor. Sensors 14 (9), 17089–17111.
Sanders, J.A., Verhulst, F., Murdock, J., 2007. Averaging Methods in Nonlinear Dynamical Systems, vol. 59, Springer.
Strogatz, S.H., 2024. Nonlinear Dynamics and Chaos: With Applications to Physics, Biology, Chemistry, and Engineering. Chapman & Hall/CRC.
Studnicka, G.M., 1987. Hyperbolic regression analysis for kinetics, electrophoresis, elisa, ria, bradford, lowry, and other applications. Bioinformatics 3 (1), 9–16.
Sun, J.Q., Xiong, F.R., Schütze, O., Hernández, C., 2018. Cell Mapping Methods. Springer.
Thompson, J.M.T., 1989. Chaotic phenomena triggering the escape from a potential well. Proc. R. Soc. A 421 (1861), 195–225.
Thompson, J.M.T., Stewart, H.B., 2002. Nonlinear Dynamics and Chaos. John Wiley & Sons.
Younis, M.I., 2011. MEMS Linear and Nonlinear Statics and Dynamics, vol. 20, Springer Science & Business Media.